Journal of Materials Chemistry A

Accepted Manuscript

ROYAL SOCIETY OF CHEMISTRY

www.rsc.org/materialsA

Journal Name

RSCPublishing

ARTICLE

High-performance $LiMnPO_4$/C nanoplates synthesized by negative pressure immersion and solid state reaction using nanoporous Mn_2O_3 precursor

Cite this: DOI: 10.1039/xoxxoooooox

Received ooth January 2015,
Accepted ooth January 2015

DOI: 10.1039/xoxxoooooox

www.rsc.org/

Jugong Zheng,[ab] Cancan Qin,[a] Tongfu Wu,[a] Shuangfei Xie,[a] Liang Ni,[a] Muyang Peng,[a] Yuefeng Tang*[a] and Yanfeng Chen[a]

Preparing high-performance $LiMnPO_4$ is still a large obstacle due to its sluggish electrochemical kinetics. To overcome this problem, a novel method is developed for $LiMnPO_4$/C nanoplates from nanoporous Mn_2O_3 precursors. There are two advantages. Firstly, through negative pressure immersion, lithium dihydrogen phosphate (LiH_2PO_4), lithium hydroxide (LiOH) and sucrose ($C_{12}H_{22}O_{11}$) are deposited on the surface of porous Mn_2O_3 nanosheets. Following solid-state reaction, three dimensional continous conductive carbon wrapped $LiMnPO_4$/C nanoplates up uniformly, which improved the conductivity greatly. Secondly, (010) exposed facets are obtained using Mn_2O_3 hierarchical microspheres as precursors, which allows for a fast transmission of Li^+ ion to improve the rate capability. As a results, as-synthesized L-Mn_2O_3-LMP/C samples exhibit a superior rate performance with discharge capacities of 157.3 mA h g^{-1} at C/20, 122.6 mA h g^{-1} at 1 C, and 105.8 mA h g^{-1} at 2 C. Meanwhile, they can retain 99.3% of the initial capacity after 100 cycles at 1C, revealing an excellent cycling stability. This method shields more light on the fabrication of high-performance $LiMnPO_4$/C cathode materials and is suitable for large scale production.

1. Introduction

Since the olivine-type was proposed as positive-electrode material for lithium ion batteries by Padhi *et al.*,[1] much research has focused on $LiMPO_4$ (M = Co, Ni, Fe or Mn) and $LiMPO_4$ compounds. Owing to a stable three-dimensional framework, lithium metal phosphate materials do not undergo a structural rearrangement during lithiation and delithiation.[1, 2] This indicates that $LiMPO_4$ electrodes may demonstrate better stability and capacity retention during prolonged cycling than layered materials. Nevertheless, the olivine family $LiMPO_4$ (M = Co, Ni, Fe or Mn) should be consider other aspects for the optimum performance in lithium ion batteries. $LiCoPO_4$ and $LiNiPO_4$ have higher redox reaction potential (>4.8 V vs. Li/Li^+) than the safer operational limit of conventional carbonate based electrolyte solutions.[3, 4] $LiFePO_4$ presents a suitable redox potential (~ 3.4 V vs. Li/Li^+), but it offers relatively lower theoretical energy density of ca. 580 W h kg^{-1}.[5, 6] Compared with the three kinds of lithium metal phosphate materials, $LiMnPO_4$ shows suitable redox potential (~ 4.1 V vs. Li/Li^+) and a higher theoretical energy density of ca. 700 Wh kg^{-1}.[7, 8] Therefore, $LiMnPO_4$ is considered as a most promising cathode material in lithium metal phosphate materials for high-energy systems such as electric or hybrid electric vehicles.[4, 9, 10]

Unfortunately, a limited rate capability is a challenge obstacle for $LiMnPO_4$ as a electrode material, which suffers from poor electronic and ionic conductivity, Jahn-Teller effects and internal stress due to lattice misfit between $LiMnPO_4$ phase and $MnPO_4$ phase.[11-13] To overcome these intrinsic drawbacks and improve the electrochemical performance, strategies including preferential growth[14-16], particle size reduction,[17-19] carbon coating,[20-24] ion-doping[25-27] etc have been employed.

Preferential growth. At first, Delacourt *et al.* synthesized ~100 nm $LiMnPO_4$ particles using a direct precipitation technique and the $LiMnPO_4$ electrode delivered a lower reversible capacity (70 mA h g^{-1} at C/20)[28]. Dong *et al.* obtained $LiMnPO_4$ nanoplates with a thickness of 50 nm via solvothermal method, but the discharge capacity was no more than 110 mA h g^{-1} at C/20. The author confirmed that the main reason for this low discharge capacity was the thickness orientation of nanoplates perpendicular to the [010] 1D Li^+ diffusion paths.[15] After that, Pan *et al.* reported that $LiMnPO_4$ microspheres assembled with plates exhibited a 130 mA h g^{-1} discharge capacity at C/20. This was attributed to the exposed (010) facets as well as the thinness along the [010] direction, which both allow for a fast Li^+ ion.[16] So preparing $LiMnPO_4$ nanoplates with the particular preferential growth along [010] direction is a effective way to improve electrochemical dynamics.

Particle size reduction. On the other hand, particle size reduction is another way to improve the rate capticy. However, $LiMnPO_4$ nanoplates are easily converted into secondary structures during the wet chemical process. As a result, the rate capability and cycling performance are hindered because of longer diffusion path for Li^+ ions. In order to obtain well dispersed $LiMnPO_4$ nanoplates, plate-like Mn-based precursors prepared during the wet chemical process are introduced in the following stages. Koleva *et al.* [29]

prepared plate-like $LiMnPO_4$ with thin plates of $KMnPO_4 \cdot H_2O$ with preferred orientation along the [010] direction. Liu *et al.* [30] used 100 ~ 300 nm thick plate-like $NH_4MnPO_4 \cdot H_2O$ as a precursor to prepare $LiMnPO_4$, which preserved the morphology of the precursor. This plate-like $LiMnPO_4$/C composite delivered a poor discharge capacity of 85 mA h g^{-1} at C/20. Bramnik *et al.* [31] synthesized $LiMnPO_4$ with a $NH_4MnPO_4 \cdot H_2O$ precursor by ion-exchange reaction. In this research, the morphology and size distribution of the precursor are preserved during ion-exchange. After ball-milling with carbon black, the granular material delivers 30% of the theoretical capacity at C/5. Kim *et al.* reported higher capacity $LiMnPO_4$ (145 mA h g^{-1} discharge capacities at C/10) synthesized with a $Mn_3(PO_4)_2$ precursor through a surface-confined precipitation process. [14] From these efforts, we can find that the specific capacity and rate capability can be improved by changing the kinds of precursors combined with suitable preparing method. Therefore, it is a significant challenge to seek a new precursor to further decrease the particle size of the $LiMnPO_4$ material for improving its capacity, especially at high rates.

Carbon coating. In terms of electrical and ionic conductivities, three-dimensional carbon matrix (electronic pathway network) could facilitate continuous electronic transport. Optimal dosage of conductive carbon is also advantageous for the diffusion or Li^+ ions.[9, 32] In general, carbon layers on cathode materials are obtained via thermal decomposition of organic carbon precursors (known as *in situ* strategies) or mechanochemical ball milling of active materials with solid carbons (known as *ex situ* strategies). [32] In the *ex situ* strategies, there is every possibility that inter-particularly connected parts in the secondary particles are blocked from the access of carbon precursors, leading to inhomogeneous coating. In comparison, *in situ* strategies could ensure a homogeneous carbon layer, becasue the probability of thermal decomposition is the same on all the primary particles. According to the *in situ* carbon coating theory, it is necessary that the Mn-based precursor should have a high specific surface area. The sufficient surface area provides the required active site for organic carbon precursors. So a kind of designed precursor with porous structure is advatage to accommodate corresponding space for the organic carbon precursors. Hence, a porous structure precursor is an optimal candidate for $LiMnPO_4$/C cathode material in *in situ* carbon coating processes.

In this article, we consider the three aspects including preferential growth, particle size reduction, and carbon coating for $LiMnPO_4$/C nanoplates preparation. And we describe a method for $LiMnPO_4$/C nanoplates using porous Mn_2O_3 nanosheets as a precursor. Mn_2O_3 microspheres assembled from porous Mn_2O_3 nanosheets were synthesized with solvothermal method. Following this, the solution immersion process under negative pressure produced a deposition layer of sucrose, lithium dihydrogen phosphate and lithium hydroxide. After solid-state reaction, $LiMnPO_4$/C nanoplates that preserved the morphology of Mn_2O_3 and exposed (010) facets were obtained successfully. For comparison, nonporous Mn_2O_3 nanoplates were also prepared using thermal treatment with commercial MnO_2 as raw material. The electrochemical performances of $LiMnPO_4$/C prepared form two kinds of Mn_2O_3 precursors were comparatively investigated. As-obtained $LiMnPO_4$/C positive electrodes do show a high reversible specific capacity, as well as excellent rate capability and cycling performance.

Experimental section

Preparation of Mn_2O_3 precursors

Synthesis of porous Mn_2O_3 sample. In a typical synthesis process, 2 mmol $Mn(CH_3COO)_2 \cdot 4H_2O$ (AR, Aladdin Chemical Reagent Co. Ltd.) and 2 g poly ethylene glycol (CR, Sinopharm Chemical Reagent Co., Ltd., Mav = 1000) were dissolved in 70 ml ethylene glycol (AR, Sinopharm Chemical Reagent Co., Ltd.). After being stirred vigorously for 30 min, the mixture was put into a 100 ml Teflon-lined stainless steel autoclave. The autoclave was treated at 180 °C and maintained for 12 h before being cooled in air. The precipitates were filtered and washed several times with absolute ethanol and dried in an oven at 60 °C. These precipitates were calcined at 600 °C for 3 h to obtain Mn_2O_3 precursors (hereafter named as L-Mn_2O_3).

Preparation of nonporous Mn_2O_3 sample. In order to prepare nonporous Mn_2O_3 nanoparticles, a typical solid-state reaction was used. Commercial γ-MnO_2 powders (AR, Aldrich) were obtained and used as the raw materials. The γ-MnO_2 powders were spread in corundum crucible and calcined at 600 °C for 12 hours in a muffle furnace. After naturally cooling to ambient temperature, the products were collected as Mn_2O_3 precursors (hereafter named as S-Mn_2O_3).

Fabrication of $LiMnPO_4$/C composites.

According to the stoichiometric molar ratio of Li : Mn = 1.03 : 1, and Li : C = 1 : 1.1, lithium dihydrogen phosphate (LiH_2PO_4, 99%, Aladdin Chemistry Co., Ltd., USA), lithium hydroxide (LiOH, 98%, Aladdin Industrial Co., China) and sucrose ($C_{12}H_{22}O_{11}$, AR, Sinopharm Chemical Reagent Co., Ltd.) were dissolved in deionized water to obtain a clear aqueous solution. The Mn_2O_3 powders were then immersed in the solution under negative pressure and produced black suspensions. Details of the processing for the suspensions are provided in supporting information (**SI 1**). The suspensions were evaporated in an ultrasonic heater. Subsequently, the dry mixtures were transferred into the tube furnace and sintered at 600 °C for 10 hours under H_2 (10%) /Ar (90%) atmosphere with a heating rate of 5 °C min^{-1}.

Materials Characterizations

The crystal structures of the products were identified using a powder X-ray diffractometer (XRD, Utima Ⅲ, Rigaku, Japan) equipped with Cu Kα radiation (λ = 0.15406 nm). The morphology was observed using a field-emission scanning electron microscopy (FE-SEM, Ultra 55, Zeiss, Germany) and a transmission electron microscopy (TEM, JEM-200CX, JEOL, Japan). The surface area was estimated with nitrogen adsorption measurement (TriStar-3000, Micromeritics, USA) at 77 K. TG-DSC was investigated on a thermal gravimetric analyser (STA449F1, NETZSCH, Germany) under nitrogen or oxygen atmosphere at a heating rate of 10 ºC min^{-1}. The percentage (wt. %) of carbon was measured using an elemental analyser (CHN-O-Rapid, Heraeus, Hanau, Germany).

Cell assembly

The electrode slurry was made by dispersing 75 wt. % $LiMnPO_4$/C, 10 wt. % acetylene black and 15 wt. % polyvinylidene fluoride (PVDF) in N-methyl-2-pyrrolidone (NMP) with magnetic stirring for 12 hours. The acquired slurry was coated uniformly on aluminum foil and dried at 120 °C in a vacuum oven to yield the

working electrode. The electrodes were then assembled into half cells in an Ar-filled glove box (MBRAUN, Germany) using Li foil as the counter electrode and Celgard 2300 membrane as the separator. The electrolyte was a solution of 1 mol L^{-1} $LiPF_6$ in ethylene carbonate (EC) and dimethyl carbonate (DMC) (v/v = 1:1).

Electrochemical Characterization

The electrochemical performances of $LiMnPO_4$/C were evaluated by galvanostatic cycling using CR2032-type coin cells. Charge–discharge experiments were conducted on an electrochemical test instrument (Maccor S4000, USA) at different current densities in a voltage range of 2.5 ~ 4.5 V. Electrochemical impedance spectroscopy (EIS) data were collected on an electro-chemical workstation (AUTOLAB PGSTAT30, Metrohm Ltd. , Switzerland) over the frequency range of 100 kHz to 0.01 Hz with an alternating voltage of 5 mV. All electrochemical measurements were carried out at room temperature.

Results and discussion

Crystalline phase and microstructure of Mn_2O_3 precursors

Fig. 1 shows XRD patterns of the precursors prepared by a solvothermal process (L-Mn_2O_3) and thermal treatment (S-Mn_2O_3). The diffraction peaks of the two patterns could be indexed to a pure cubic phase of Mn_2O_3, which is in good agreement with the standard values (JCPDS: 41-1442).

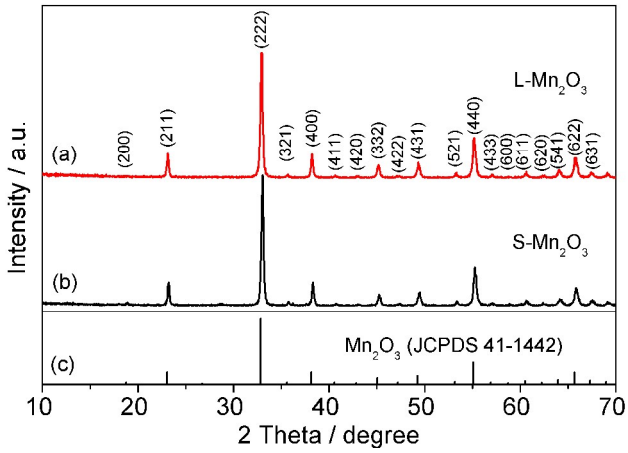

Fig.1 XRD patterns of the L-Mn_2O_3 prepared by the solvothermal process and S-Mn_2O_3 prepared with heat treatment, (a) L-Mn_2O_3, (b) S-Mn_2O_3, (c) the standard JCPDS card: No. 41-1442 of Mn_2O_3.

During the solvothermal process, manganese glycolates (Mn-EG) were formed by alcoholysis and coordination of ethylene glycol with the manganese ions.[33] The XRD patterns of Mn-EG are shown in supporting information (**SI Fig. 1**). Several Mn-EG molecules are coordinated into various size nanosheets. Meanwhile, Mn-EG nanoplates are assembled into secondary microspheres under the template action of polyethylene glycol (PEG) micelles. After the thermal treatment, Mn-EG was decomposed into uniform L-Mn_2O_3 hierarchical microspheres (Fig. $2a_1$). The SEM image of single microspheres (insert of Fig. $2a_1$) and TEM image (Fig. $2a_2$) show that the nanosheets carry a large number of pores. This is ascribed to the dissolution of PEG during precipitate washing and the combustion of organic components during the thermal treatment. TEM images (Fig. $2a_3$, $2a_4$) further demonstrates that the L-Mn_2O_3 nanosheets consist of irregular nanopaltes with a width of ~30nm and pores derived from the elimination of organisms. In comparison, commercial ramsdellite MnO_2 (*R*-MnO_2) particles show irregular morphology as shown in the supporting information (**SI Fig. 2**). After the heat-treatment process under an air atmosphere, *R*-MnO_2 were transformed into cubic phase S-Mn_2O_3 due to oxygen emission.[34] The SEM image (Fig. $2b_1$) and TEM images (Fig. $2b_2$, $2b_3$) demonstrate that S-Mn_2O_3 particles are composed of nonporous nanoparticles. Moreover, HRTEM image (Fig. $2b_4$) more clearly reveals an overview of crystalline characteristic, the interplanar spacing of 0.384(1) nm corresponds to (211) lattice planes of the cubic phase of Mn_2O_3.

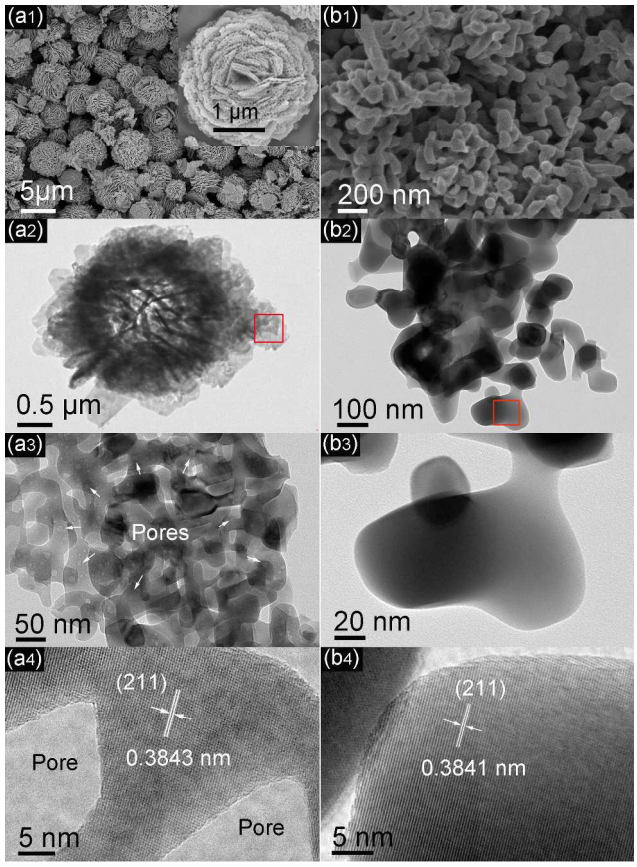

Fig. 2 SEM and TEM images of the two as-prepared precursors, a_1, a_2, a_3 and a_4 are SEM, TEM and HRTEM images of L-Mn_2O_3 precursors, respectively. b_1, b_2, b_3 and b_4 are SEM, TEM and HRTEM images of S-Mn_2O_3 precursors, respectively.

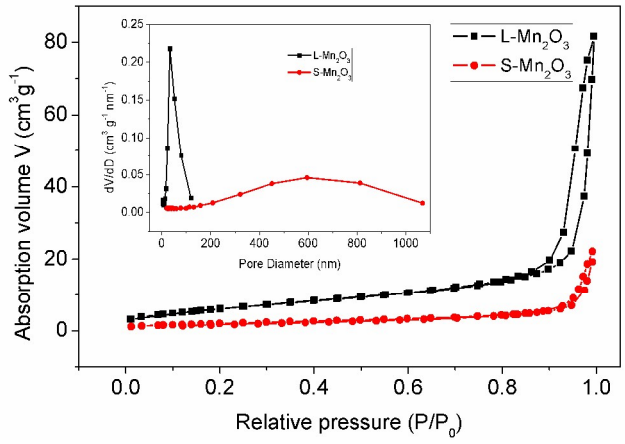

Fig. 3 N_2 adsorption/desorption isotherm (77 k) curve of L-Mn_2O_3, porous volume distributions of the pore size (the inset picture).

The Brurauer–Emmerr–Teller (BET) surface area of L-Mn_2O_3 and L-Mn_2O_3 were analysed by N_2 sorption isotherms shown in Figure 3. The BET surface area of L-Mn_2O_3 and S-Mn_2O_3 are 22.8 m^2 g^{-1} and 7.3 m^2 g^{-1}, respectively. L-Mn_2O_3 exhibits a type IV isotherm with H3-type hysteresis at high relative pressures, indicating the existence of mesopores between the primary particles. The hysteresis at high relative pressures of S-Mn_2O_3 indicates the existence of mesopores and macropores. The inset shows Barrett–Joyner–Halenda (BJH) pore size distribution derived from the adsorption branch of the isotherm. It is sure that L-Mn_2O_3 possesses a narrow pore size distribution with an average size of 30 nm. And S-Mn_2O_3 presents a broad pore size distribution. These results are consistent with the TEM image (Fig. 2a_3). The L-Mn_2O_3 hierarchical microspheres provide larger interface and better penetration of the solution.

Crystalline phase and microstructure of $LiMnPO_4$/C nanoplates

Fig. 4 plots XRD patterns of the as-synthesized $LiMnPO_4$/C samples by solid-state reaction from two precursors L-Mn_2O_3 and S-Mn_2O_3. All diffraction peaks of the two patterns could be indexed to the orthorhombic olivine structure with a *Pnma* space group (JCPDS card No. 74-0375). However, the characteristic peak intensities of the two patterns show a significant difference. Especially, the peak intensity ratio between (020) and (200) peaks, I_{200}/I_{020} value is 3.28 and 2.61 for L-Mn_2O_3-LMP/C and S-Mn_2O_3-LMP/C, respectively. I_{200}/I_{020} of L-Mn_2O_3-LMP/C is higher than 2.64 for the standard JCPDS card No.74-0375. In the olivine structure, the peak intensity ratio is recognized as an important characteristic to indicate the oriented growth with plate-like morphology.[35] This is favorable for the lithium ions diffusion along the b axis in the bulk due to the unique 1D ion diffusion channel, which indicates the obtained L-Mn_2O_3-LMP/C samples might have a plate-like morphology. This will be further checked using SEM and TEM technology.

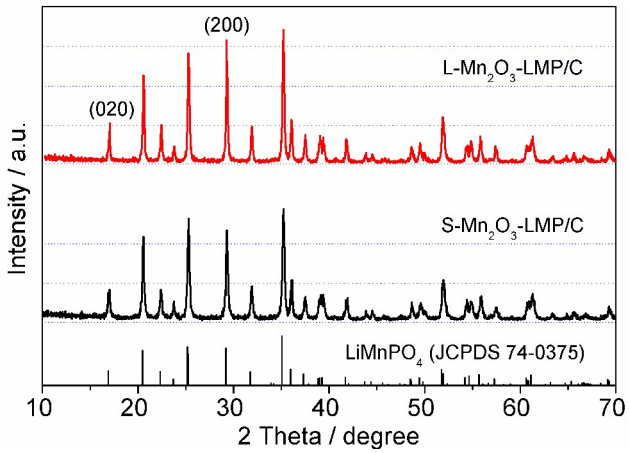

Fig. 4 XRD patterns of the as-synthesized samples by solid-state reaction with different precursors, L-Mn_2O_3-$LiMnPO_4$/C prepared from L-Mn_2O_3 precursors and S-Mn_2O_3-$LiMnPO_4$/C prepared from S-Mn_2O_3 precursors.

Fig. 5 shows FE-SEM, TEM，HRTEM images and SAED patterns of $LiMnPO_4$/C prepared from two kinds of precursors. For L-Mn_2O_3-LMP/C samples, Fig. 5a_1 reveals hierarchical nanosheets assembled from plate-like primary granules. The inset shows the primary granules are approximatively polygonous nanoplates. By contrast, the S-Mn_2O_3-LMP/C samples (as shown in Fig. 5b1, 5b2) have significant aggregation and a broad size distribution. The SAED technique was used to analyse the crystallographic orientation of the L-Mn_2O_3-LMP/C nanoplates by orienting the incident beam directly perpendicular to the nanoplates. The corresponding SAED pattern is shown in Fig. 5a_3. The (001) and (101) reciprocal lattice vectors of olivine $LiMnPO_4$ span the reciprocal lattice and indicate that this SAED pattern is taken close to the [010] zone axis, which means the thin side of the nanoplate is along the [010] direction. To further confirm the horizontal face of the L-Mn_2O_3-LMP/C nanoplates, the structures along the direction perpendicular to the nanoplates were also characterized by HRTEM. Fig. 5a_4 is an HRTEM image taken for the nanoplates in Fig. 5a_2. The fringe spacing values are measured to be about 0.305(0) nm, 0.237(2) nm and 0.374(4) nm, which are in good agreement with the (200), (002) and (101) crystalline planes of orthorhombic phase $LiMnPO_4$ with a Pnma space group, respectively. It shows that the L-Mn_2O_3-LMP/C nanoplates expose the (010) plane, which is perpendicular to the (200) and (002) planes. This result agrees well with the SAED pattern. It reveals that the $LiMnPO_4$ nanoplates expose a large (010) face, and the [010] direction is just the thinnest part of the nanoplates, which benefit for the migration of Li ions.[36] Fig.5b_3, 5b_4 present the SAED pattern and HRTEM of S-Mn_2O_3-LMP/C, which is also consistent to the crystal structure of $LiMnPO_4$.

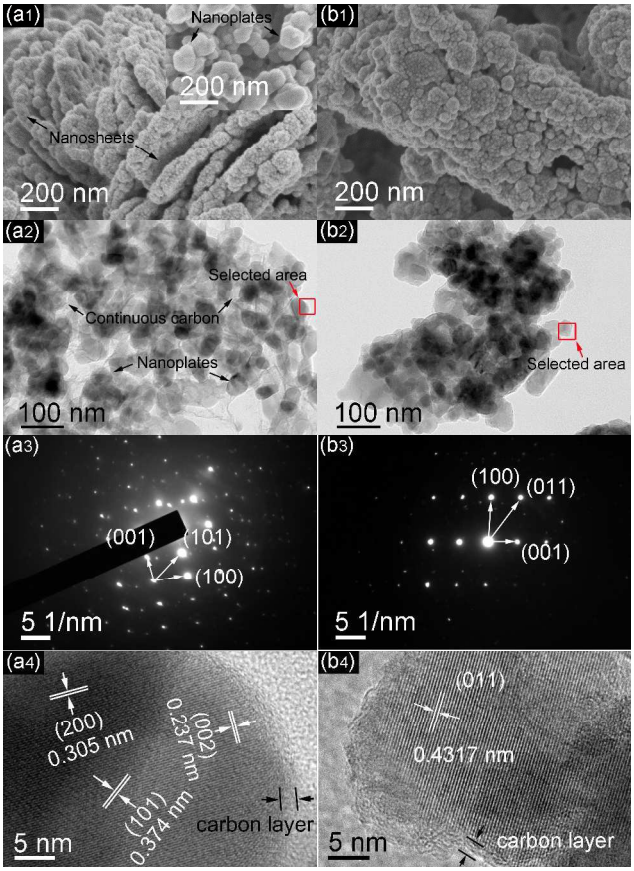

Fig. 5 SEM, TEM, HRTEM images and SAED patterns. Fig.5a_1, 5a_2, 5a_4, 5a_3 are SEM, TEM, HRTEM images and SAED patterns of L-Mn_2O_3-$LiMnPO_4$/C samples, respectively. 5b_1, 5b_2, 5b_4, 5b_3 are SEM, TEM, HRTEM and and SAED patterns images of S-Mn_2O_3-$LiMnPO_4$/C samples, respectively.

As far as carbon coating is concerned, it can be clearly seen from Figure 5a_2 that continuous carbon located between plates so that the plates were interconnected by a uniformly distributed carbon network. This three-dimensional conductive carbon is attributed to the *in situ* caoting carbon. During the negative pressure immersion, a large number of pores of L-Mn_2O_3 microsphere were opened. Subsequently, LiOH, LiH_2PO_4 and $C_{12}H_{22}O_{11}$ molecules were uniformly deposited on the surface of the primary particles along with the solution infiltration. In response to uniform deposition layer of sucrose, L-Mn_2O_3-LMP/C samples (Figure 4b_4) possess more uniform carbon layer than that of S-Mn_2O_3-LMP/C samples. Considering the effect of the carbon content on the connection between $LiMnPO_4$ and carbon networks,[37] L-Mn_2O_3-LMP/C and S-Mn_2O_3-LMP/C were prepared with same amounts of sucrose. The results of elemental analyzer show the carbon contents in L-Mn_2O_3-LMP/C and S-Mn_2O_3-LMP/C are about 8.16 wt% and 6.93 wt%, respectively. It indicates more carbon was consumed in the carbon thermal reduction for S-Mn_2O_3-LMP/C than that for L-Mn_2O_3-LMP/C samples.

Electrochemical performances of $LiMnPO_4$/C cathode materials

Fig. 6a shows the initial charge-discharge curves of L-Mn_2O_3-LMP/C and S-Mn_2O_3-LMP/C. Two cells were charged at C/20 (8.5 mA g^{-1}) to 4.5 V and kept at this voltage until the current decreased to C/200, and then discharged at C/20 to 2.5 V. It is evident that the flat redox potential is around 4.1 V (vs. Li/Li^+). The polarization between the initial charge/discharge plateaus was only approximately 200 mV and the flat charge/discharge plateaus indicated improved kinetics. And the discharge capacities are 157.3 and 159.2 mA h g^{-1} for the L-Mn_2O_3-LMP/C and S-Mn_2O_3-LMP/C, respectively. This is superior to discharge capacities reported previously in the state-of-art research.[7, 19, 37] For the rate test, the cell was charged at C/10 to a cut-off voltage of 4.5 V and kept at this voltage until the current decreased to C/100, and then discharged at different rates to 2.5 V from 0.1 C to 10 C. As shown in Fig. 6b, L-Mn_2O_3-LMP/C presents better rate performance than the S-Mn_2O_3-LMP/C sample. It delivered a superior discharge capacity of 146.3 mA h g^{-1} at C/10. With the increase of discharge current, the specific capacity decreased gradually and exhibited 130.9 mA h g^{-1} when the discharge rate increased to C/2. At high current rates of 2 C and 3 C, specific capacities of 98.2mA h g^{-1} and 71.1mA h g^{-1} are obtained, corresponding to 67.1% and 48.6% of the cell's reversible capacity respectively.

The discharge profiles of the two samples at different rates are shown in Fig. 6c and Fig. 6d. The lowering of discharge curves at higher rates is due to the polarization of the cell induced by the internal resistance of the cell.[38, 39] The appreciable plateau is maintained around 4.0 V until C/5, reflecting the low internal resistance of the L-Mn_2O_3-LMP/C material. In comparison, the rate capacity of the S-Mn_2O_3-LMP/C lagged far behind the L-Mn_2O_3-LMP/C material. Although S-Mn_2O_3-LMP/C delivered a considerable specific capacity at low rates, a discharge capacity of less than 100 mA h g^{-1} at 1 C was delivered. When the rate increased to 5 C, almost no electrochemical activity was obtained, implying sluggish lithium ions transfer in the bulk $LiMnPO_4$ particles. The superior rate capability of L-Mn_2O_3-LMP/C is mainly attributed to the improved electronic conductivity arising from the continuous conductive carbon and facile diffusion of lithium ions in the $LiMnPO_4$ structure due to the greatly shortened diffusion path. This demonstrates the importance of well-distributed *situ* coating carbon for the improvement of electrochemical performance. The cycling performance curves of the two samples at different rates are shown in Fig. 6e. In the cycling test, two test stages were applied. In the first 100 cycles, each cell was charged at C/10 to a cut-off voltage of 4.5 V and kept at this voltage until the current decreased to C/100, and then discharged at C/10 to 2.5 V. In the following 100 cycles, cells were charged at C/10 and discharged at 1 C. It can be seen that L-Mn_2O_3-LMP/C showed stable capacity and only slight capacity fade was observed after 200 cycles. The initial capacity was 140 mA h g^{-1} and 98% of the capacity was maintained after 100 cycles. When the charge–discharge rates were raised to 0.1 C/1 C, the capacity retention for the second 100 cycles was 99.3%. By contrast, an obvious capacity fade was observed in the whole cycle for S-Mn_2O_3-LMP/C. It may be due to the continual side reaction.[39] Owing to the Jahn-Teller distortion, the large aggregations are cracked, engendering a new active surface area of $LiMnPO_4$ to the electrolyte. Side reaction occurs at the electrode–electrolyte interface, resulting in a slight loss of active material and capacity fading. The stable electrochemical cycling of L-Mn_2O_3-LMP/C, as mentioned above, is associated with the high crystallinity resulting from the solid-state method and the intrinsic combination between primary $LiMnPO_4$ granule and the well-distributed conductive carbon.

To further clarify the difference in the electrochemical properties of two the LMP/C samples, electrochemical impedance spectroscopy (EIS) measurement of the coin cells was carried out after the rate test. Fig. 6f shows the EIS spectra for the L-Mn_2O_3-LMP/C and S-

Mn_2O_3-LMP/C materials in the activated cells and corresponding equivalent circuits. It can be seen that each curve is composed of a depressed semicircle in the high-to-medium frequency region and a sloping line of Warburg impedance in the low frequency region. The semicircle can be divided into two parts, high frequency and medium frequency. The former relates to the formation of EIS films on the surface of the electrode and the latter corresponds to the charge-transfer process. [40] The simulation results based on the equivalent circuits show that the charge-transfer resistance (Rct) values are 95.7 Ω and 190.1 Ω for L-Mn_2O_3-LMP/C and S-Mn_2O_3-LMP/C respectively. The lower Rct value of the L-Mn_2O_3-LMP/C electrode indicates that it has better charge transfer kinetics, which is consistent with the better reversible capacities and rate performance. The Warburg impedance relates to the diffusion of lithium ions within the electrode. In order to investigate the diffusion of Lithium ions in the active materials, the diffusion coefficient of lithium ions (D_{Li}) is calculate according to the following equation:

$$D_{Li} = \frac{R^2T^2}{2A^2n^4F^4C^2\sigma^2}$$

Where R is the gas constant, T is the absolute temperature, A is the surface area of the electrode, n is the number of electrons per molecule during oxidization, F is the Faraday constant, C is the concentration of Lithium ions and σ is the Warburg factor. The value of σ is the slope of the lines between Z′ and $\omega^{-1/2}$, as shown in the inset of Fig. 6f. Accordingly, the D_{Li} of L-Mn_2O_3-LMP/C and S-Mn_2O_3-LMP/C were determined to be 9.28×10^{-13} and 2.16×10^{-13} cm^2 S^{-1} respectively. The diffusion of lithium ions for L-Mn_2O_3-LMP/C is faster than that of S-Mn_2O_3-LMP/C. this can be attributed to the much shortened diffusion path, as discussed in the TEM section of this paper. Thus, the EIS results are consistent with the superior electrochemical performance of L-Mn_2O_3-LMP/C.

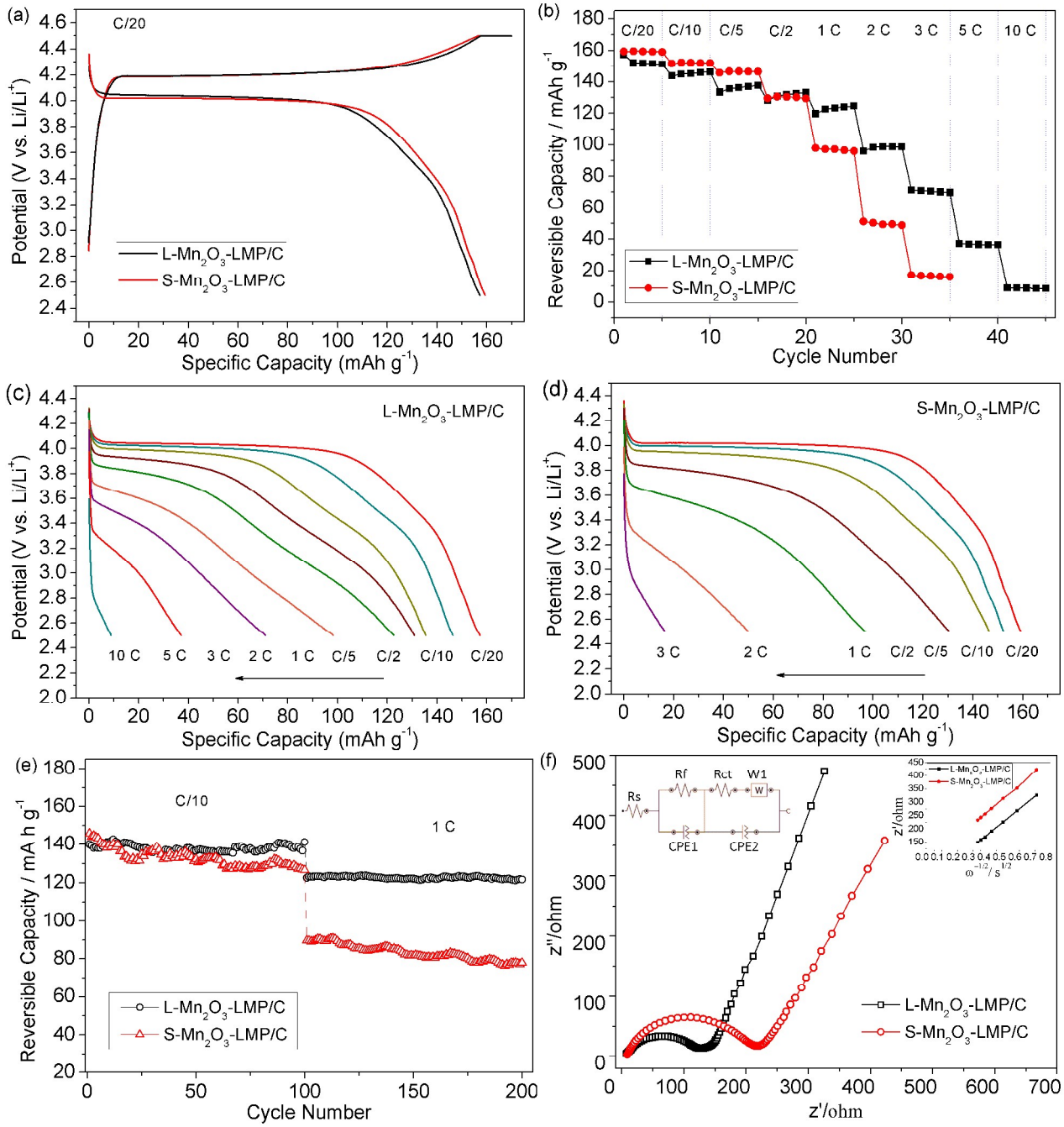

Fig. 6 (a) The initial charge–discharge curves of L-Mn_2O_3-$LiMnPO_4$/C and S-Mn_2O_3-$LiMnPO_4$/C. (b) Rate capability of L-Mn_2O_3-$LiMnPO_4$/C and S-Mn_2O_3-$LiMnPO_4$/C at different discharge rates. The cell was charged at a constant current rate of C/10 to 4.5 V and kept at 4.5 V until C/100, then discharged at different rates to 2.5 V. (c) The discharge profiles of L-Mn_2O_3-$LiMnPO_4$/C at different rates. (d) The discharge profiles of S-Mn_2O_3-$LiMnPO_4$/C at different rates. (e) Cycling performance of L-Mn_2O_3-$LiMnPO_4$/C and S-Mn_2O_3-$LiMnPO_4$/C at a discharge rate of 0.1Cand 0.5Cfor 50 cycles, respectively. (f) Impedance spectra of L-Mn_2O_3-$LiMnPO_4$/C and S-Mn_2O_3-$LiMnPO_4$/C after the rate test and corresponding equivalent circuit. The inset shows the plots of the real resistance as a function of the inverse square root of angular frequency.

Conclusions

In this article, we developed a novel method to prepare $LiMnPO_4$/C from porous Mn_2O_3 precursors. Combined a negative pressure immersion with solid-state reaction, we have prepared $LiMnPO_4$/C nanoplates with continuous 3D conductive carbon and exposed (010) facets, which improve the conductivity and the rate of the migration of Li ions greatly. For comparation, Mn_2O_3 nanoparticles prepared from commercial MnO_2 show apparent aggregations. Consequently, phosphate and sucrose precipitated from mixed solution are only deposited on the surface of the secondary particles. As a results, L-Mn_2O_3-LMP/C samples exhibit a superior rate performance with discharge capacities of 157.3 mA h g^{-1} at C/20, 122.6 mA h g^{-1} at 1 C, and 105.8 mA h g^{-1} at 2 C. Meanwhile, they can retain 99.3% of the initial capacity after 100 cycles at 1C, revealing an excellent cycling stability.This

new synthesis strategy has great potential for the synthesis of other different materials with extremely low electrical conductivity for various energy-storage devices.

Acknowledgements

This research was supported by Jiangsu Province prospective joint research on pilot project (No.:BY2013072-03), a Grant for State Key Program for Basic Research of China (Nos.: 2013CB632702, 2012CB921503), the National Natural Science Foundation of China (No.:11134006, 11374149), A Project funded by the Priority Academic Program Development of Jiangsu Higher Education Institutions (PAPD), Jiangsu Province college graduate research and innovation projects (CXLX13-042), a Project of Free Exploration funded by National Laboratory of Solid State Microstructures, Test Foundation of Nanjing University.

Notes

[a] National Laboratory of Solid State Microstructures and Department of Materials Science and Engineering, College of Engineering and Applied Sciences, Nanjing University, Nanjing 210093, China
[b] Department of Materials Science and Engineering, East China Institute of Technology, Nanchang 330013, China.
*Corresponding author 1, Yuefeng Tang. E-mail address: yftang@nju.edu.cn.

References

1. A. K. Padhi, K. S. Nanjundaswamy and J. B. Goodenough, *J. Electrochem. Soc.*, 1997, **144**, 1188-1194.
2. S. K. Martha, B. Markovsky, J. Grinblat, Y. Gofer, O. Haik, E. Zinigrad, D. Aurbach, T. Drezen, D. Wang, G. Deghenghi and I. Exnar, *J. Electrochem. Soc.*, 2009, **156**, A541-A552.
3. S. Okada, S. Sawa, M. Egashira, J. Yamaki, M. Tabuchi, H. Kageyama, T. Konishi and A. Yoshino, *J. Power Sources*, 2001, **97-98**, 430-432.
4. V. Aravindan, J. Gnanaraj, Y. S. Lee and S. Madhavi, *J. Mater. Chem. A*, 2013, **1**, 3518-3539.
5. A. Yamada, S. C. Chung and K. Hinokuma, *J. Electrochem. Soc.*, 2001, **148**, A224-A229.
6. B. Rong, Y. Lu, X. Liu, Q. Chen, K. Tang, H. Yang, X. Wu, F. Shen, Y. Chen, Y. Tang and Y. Chen, *Nano Energy*, 2014, **6**, 173-179.
7. D. Choi, D. Wang, I. T. Bae, J. Xiao, Z. Nie, W. Wang, V. V. Viswanathan, Y. J. Lee, J. G. Zhang, G. L. Graff, Z. Yang and J. Liu, *Nano lett.*, 2010, **10**, 2799-2805.
8. D. Choi, J. Xiao, Y. J. Choi, J. S. Hardy, M. Vijayakumar, M. S. Bhuvaneswari, J. Liu, W. Xu, W. Wang, Z. Yang, G. L. Graff and J.-G. Zhang, *Energy Environ. Sci.*, 2011, **4**, 4560.
9. H. Yoo, M. Jo, B.-S. Jin, H.-S. Kim and J. Cho, *Adv. Energy Mater.*, 2011, **1**, 347-351.
10. J. Xu, S. Dou, H. Liu and L. Dai, *Nano Energy*, 2013, **2**, 439-442.
11. C. Delacourt, L. Laffont, R. Bouchet, C. Wurm, J. B. Leriche, M. Morcrette, J. M. Tarascon and C. Masquelier, *J. Electrochem. Soc.*, 2005, **152**, A913.
12. M. Yonemura, A. Yamada, Y. Takei, N. Sonoyama and R. Kanno, *J. Electrochem. Soc.*, 2004, **151**, A1352-A1356.
13. H. C. Dinh, S. I. Mho, Y. Kang and I. H. Yeo, *J. Power Sources*, 2013, **244**, 189-195.
14. T. H. Kim, H. S. Park, M. H. Lee, S. Y. Lee and H. K. Song, *J. Power Sources*, 2012, **210**, 1-6.
15. Y. Z. Dong, H. Xie, J. Song, M. W. Xu, Y. M. Zhao and J. B. Goodenough, *J. Electrochem. Soc.*, 2012, **159**, A995-A998.
16. X. L. Pan, C. Y. Xu and L. Zhen, *CrystEngComm*, 2012, **14**, 6412.
17. T. Drezen, N. H. Kwon, P. Bowen, I. Teerlinck, M. Isono and I. Exnar, *J. Power Sources*, 2007, **174**, 949-953.
18. Z. Pei, X. Zhang and X. Gao, *J. Alloys Compd.*, 2013, **546**, 92-94.
19. Y. T. Cui, N. Xu, L. Q. Kou, M. T. Wu and L. Chen, *J. Power Sources*, 2014, **249**, 42-47.
20. Z. Bakenov and I. Taniguchi, *J. Power Sources*, 2010, **195**, 7445-7451.
21. P. R. Kumar, M. Venkateswarlu, M. Misra, A. K. Mohanty and N. Satyanarayana, *J. Electrochem. Soc.*, 2011, **158**, A227-A230.
22. J. L. Liu, X. Y. Liu, T. Huang and A. S. Yu, *J. Power Sources*, 2013, **229**, 203-209.
23. J. G. Duan, Y. B. Cao, J. B. Jiang, K. Du, Z. D. Peng and G. R. Hu, *J. Power Sources*, 2014, **268**, 146-152.
24. J. Zheng, L. Ni, Y. Lu, C. Qin, P. Liu, T. Wu, Y. Tang and Y. Chen, *J. Power Sources*, 2015, **282**, 444-451.
25. D. Y. Wang, C. Y. Ouyang, T. Drezen, I. Exnar, A. Kay, N. H. Kwon, P. Gouerec, J. H. Miners, M. K. Wang and M. Gratzel, *J. Electrochem. Soc.*, 2010, **157**, A225-A229.
26. J. F. Ni and L. J. Gao, *J. Power Sources*, 2011, **196**, 6498-6501.
27. V. Ramar and P. Balaya, *Phys. Chem. Chem. Phys.*, 2013, **15**, 17240-17249.
28. P. P. C. Delacourt, M. Morcrette, J.-M. Tarascon, and C. Masquelier, *chem. mater.*, 2004, **16**, 93-99.
29. V. Koleva, E. Zhecheva and R. Stoyanova, *Dalton Trans*, 2011, **40**, 7385-7394.
30. J. L. Liu, D. G. Hu, T. Huang and A. S. Yu, *J. Alloys Compd.*, 2012, **518**, 58-62.
31. N. N. Bramnik and H. Ehrenberg, *J. Alloy Compd.*, 2008, **464**, 259-264.
32. H. S. Park, T. H. Kim, M. H. Lee and H. K. Song, *J. Mater. Chem.*, 2012, **22**, 20305-20310.
33. L. Hu, Y. Sun, F. Zhang and Q. Chen, *J.Alloys Compd.*, 2013, **576**, 86-92.
34. E. M. Otto, *J. Electrochem.l Soc.*, 1965, **112**, 367-&.
35. K. Dokko, S. Koizumi, H. Nakano and K. Kanamura, *J. Mater. Chem.*, 2007, **17**, 4803-4810.
36. H. Guo, C. Y. Wu, J. Xie, S. C. Zhang, G. S. Cao and X. B. Zhao, *J. Mater. Chem. A*, 2014, **2**, 10581-10588.
37. S. M. Oh, S. W. Oh, C. S. Yoon, B. Scrosati, K. Amine and Y. K. Sun, *Adv. Funct. Mater.*, 2010, **20**, 3260-3265.
38. H. H. Zheng, R. Z. Yang, G. Liu, X. Y. Song and V. S. Battaglia, *J. Phys. Chem. C*, 2012, **116**, 4875-4882.
39. L. F. Zhang, Q. T. Qu, L. Zhang, J. Li and H. H. Zheng, *J. Mater. Chem. A*, 2014, **2**, 711-719.
40. Y. J. Zhu and C. S. Wang, *J. Power Sources*, 2011, **196**, 1442-1448.

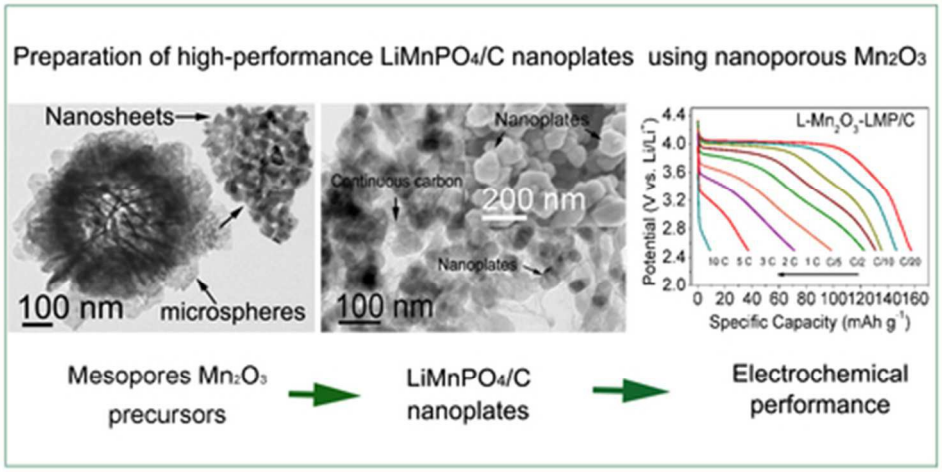

Preparation of high-performance LiMnPO4/C nanoplates using nanoporous Mn2O3
39x19mm (300 x 300 DPI)